

Nature of Infrared Sources in 11 μm Selected Sample from Early Data of the AKARI North Ecliptic Pole Deep Survey

Hyung Mok LEE¹, Myungshin IM¹, Takehiko WADA² Hyunjin SHIM¹, Seong Jin KIM¹, Myung Gyoon LEE¹

arXiv:0705.1387v2 [astro-ph] 10 Aug 2007

(Received –; accepted –)

Abstract

We present the properties of 11 μm selected sources detected in the early data of the North Ecliptic Pole Deep (NEP-Deep) Survey of AKARI. The data set covers 6 wavelength bands from 2.5 to 11 μm , with the exposure time of 10 \sim 20 minutes. This field lies within the CFHT survey with four filter bands (g', r', i', z'), enabling us to establish nearly continuous spectral energy distributions (SEDs) for wavelengths ranging from 0.4 to 11 μm . The main sample studied here consists of 72 sources whose 11 μm AB magnitudes are equal to or brighter than 18.5 (251 μJy), which is complete to more than 90%. The 11 μm band has an advantage of sampling star forming galaxies with low to medium redshifts since the prominent PAH feature shifts into this band. As expected, we find that the majority (69%) of 11 μm bright sources are star forming galaxies at $0.2 \lesssim z \lesssim 0.7$ with $L_{IR} \sim 10^{10} - 10^{12} L_{\odot}$ based on the detailed modelling of SEDs. We also find four AGNs lying at various redshifts in the main sample. In addition, we discuss a few sources which have non-typical SEDs of the main sample, including a brown dwarf candidate, a steep power-law source, flat spectrum object, and an early-type galaxy at moderate redshift.

Key words: galaxies: evolution – galaxies: formation – infrared: galaxies –

1. INTRODUCTION

AKARI is an infrared space telescope, which was launched in February 2006, in order to carry out all sky survey at mid- to far-infrared (Murakami 1998; Nakagawa 2001, Shibai 2004). In addition to the all sky survey, AKARI is capable of making pointed observations at near- to far-infrared. Because of the nature of the sun-synchronous polar orbit, North and South Ecliptic Polar regions (NEP and SEP, hereafter) have very good visibility so that repeated exposures are possible. In particular, an extragalactic survey of the NEP region has been designed to perform the deep imaging of pre-selected blank field from 2.5 to 26 μm in order to study the formation and evolution of galaxies. More details of the deep extragalactic NEP survey (hereafter, NEP-Deep) and its strategies can be found in Matsuhara et al. (2006). Currently, we are planning to release the NEP survey data to public in 2008, approximately one year after the completion of the survey.

Prior to the full, complete NEP survey, mini surveys have been carried out in order to assess the capabilities of AKARI. One of them is an imaging survey called the NEP-deep-early survey. The NEP-deep-early field covers two fields of views, one with the MIR-L camera (L15, L18W, and L24 bands), and another with the NIR and the MIR-S cameras with 6 bands covering 2.5 to 11 μm , at the total accumulated on-source exposure time of 10 to 20 minutes using IRC05 Astronomical Observation Template (AOT) (Onaka et al. 2007). The size of each field is roughly $10' \times 10'$.

The NIR/MIR-S part is covered by the CFHT Megaprime optical survey at g' , r' , i' , and z' bands (Hwang et al. 2007). Other mini surveys include the NEP monitor field survey taken with a different observing mode, and the AKARI/NEP performance verification (NEP-PV) field survey.

The purpose of the current paper is to examine the properties of the infrared sources detected in the NIR/MIR-S part of the NEP-deep-early survey field. While other survey fields provide a wider wavelength coverage (the NEP monitor field survey) or different wavelength information (L15; NEP-PV survey), the NEP-deep-early field data can provide with the complementary information regarding the nature of infrared sources expected in the NEP wide survey which has a similar survey depth to this data set but with much wider areal coverage. Analysis of an independent field also provides an opportunity to discover interesting rare sources. In particular, we will study in this paper, the nature of 11 μm selected objects. Related topics will be covered by other papers: detailed analysis of the monitor field data (Takagi et al. 2007), the optical identification of 15 μm selected sources (Matsuhara et al. 2007), the source counts in N3, S7, and L15-bands (Wada et al. 2007), and X-ray sources in the NEP survey data (Oyabu

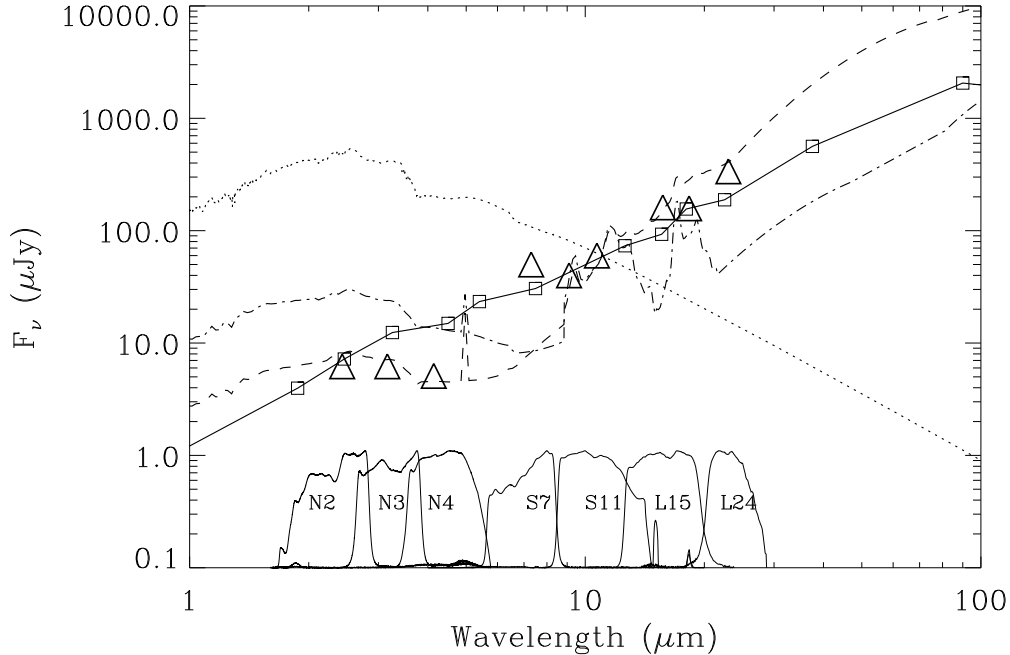


Fig. 1. Spectral energy distribution of various sources normalized to the AKARI IRC detection limits of our data at $11 \mu\text{m}$. Different lines represent SEDs of different types of galaxies at $z = 0.5$ which is a typical redshift of $11 \mu\text{m}$ sources: a passively evolving galaxy with the age of 2.5 Gyr (dotted line), a galaxy with moderate star formation rate like typical disk galaxies (dot-dashed line), infrared luminous starburst galaxy similar to Arp220 (dashed line), and an AGN, Mrk231 (small squares connected with solid lines). Also plotted are the detection limits (triangles), and the filter response curves. This figure demonstrates that S11 is effective at picking up the PAH feature of a moderate redshift star-forming galaxy. Note that S9W covers the spectral responses of S7 and S11.

et al. 2007).

Among the six wavelength bands of the NEP-deep-early survey data, the $11 \mu\text{m}$ image has been used in the primary selection of the sample. The S11 passband samples the wavelength red-ward of the Spitzer IRAC channel 4 ($8 \mu\text{m}$) from $8 \mu\text{m}$ to $15 \mu\text{m}$, filling in a gap in the Spitzer passbands. At $11 \mu\text{m}$, there is a strong silicate absorption in star forming galaxies at $z = 0$, but the S11 band is also where the strong PAH features at 6.3 and $7.7 \mu\text{m}$ redshift into at $0.2 \lesssim z \lesssim 0.7$ (Fig. 1). Therefore, unlike source selections based on an $8 \mu\text{m}$ band (e.g., the Spitzer IRAC Channel 4), the $11 \mu\text{m}$ sources are likely to be dominated by the star-forming galaxies at redshift in the range $0.2 \sim 0.7$. Previous studies of IR luminous galaxies and star formation activities using the *Spitzer* data have relied upon the extrapolation of the 8 micron and 24 micron bands, which can introduce a significant uncertainty in the estimate of IR luminosity. With the unique capability of the $11 \mu\text{m}$ imaging of AKARI, we should be able to reduce such an uncertainty in understanding the IR activity of galaxies at moderate redshifts. Other sources that can be found in the $11 \mu\text{m}$ include Active Galactic Nuclei (AGNs)

Table 1. Observational Parameters of NEP Early Data

Filter Name	Effective Wavelength (μm)	Total Integration Time (sec)	Detection Limit (5σ , μJy : Estimates)
N2	2.43	654.5	6.2
N3	3.16	981.7	6.2
N4	4.14	589.1	5.1
S7	7.19	1227.0	50
S9W	8.74	768.5	40
S11	10.4	687.1	60

and stars.

In this work, we characterize properties of objects selected based upon this new wavelength regime. This paper is organized as follows. In the immediately following section, we describe the details of the NEP-deep-early survey data set. In §3, we present the results of the photometry on the data. The characteristics of the infrared sources in conjunction with other available data are discussed in detail in §4. In addition to the 11 μ flux limited sample, we also find sources that need special attention based on the SEDs in other bands. Such objects are discussed in §5. The final section summarizes our main results. Throughout this paper, we will use AB magnitude system which converts to μJy as $\text{ABmag}=23.9 - 2.5\log_{10}[\text{Flux}(\mu\text{Jy})]$.

2. NEP-DEEP-EARLY SURVEY DATA

The NEP-deep-early survey data have been taken during the early phase of the scientific observations that started in early May 2006 in order to assess the performance of the IRC instrument (Onaka et al. 2007). The passbands covered by this mini survey are N2, N3, N4, S7, S9W, and S11 (see Matsuhara et al. 2006 for the detailed information on the designation of the filters). Our field is centered on $\alpha = 17^{\text{h}}56^{\text{m}}48^{\text{s}}$, $\delta = +66^{\circ}09'49''$ with approximately $10' \times 10'$ field of view. This area lies within the proposed NEP-Deep survey of 0.5 deg^2 circular field centered on $\alpha = 17^{\text{h}}55^{\text{m}}24^{\text{s}}$, $\delta = +66^{\circ}37'32''$.

The data were taken with the IRC05 AOT mode which uses a rather small number of resets per pointing opportunity that lasts for about 10 minutes in order to achieve deep imaging. This AOT also uses Fowler 16 data reading scheme which increases the signal-to-noise ratio significantly. The effective on-source exposure time of 1 pointing observation is a bit over 5 minutes. The observing parameter of each pointing is listed in Table 1.

The frames taken in a single observing session that lasts for about 10 minutes are processed and stacked by using the IRC data reduction pipeline version 070104 (Ita et al. 2007). Within this pipeline, the anomalous pixels have been clipped, dark signals have been subtracted with the darks taken in each pointing observation (self-dark), and the linearity correction has

been carried out. The optical distortion due to off-axis imaging has also been corrected for. The cosmic rays have been removed at this stage.

The images taken during different pointing observations have been co-added by using SWarp¹. The result of the coadded master image at S11 band is shown in Fig. 2, together with the g-r-i color composite of the optical image taken with the CFHT Megaprime (Hwang et al. 2007). The depth of the optical data is 26.1, 25.6, 24.9, and 23.7 AB magnitude at $4\text{-}\sigma$ over an $1''.0$ aperture in g' , r' , i' , and z' bands. The optical data allow us to provide further morphological information on the sources detected in the infrared. We use the CFHT data set for identification of infrared sources as well as to construct continuous SEDs of detected sources from optical to mid-infrared wavelengths.

3. Detection and Selection of Sources

Source detection was done by using SExtractor (Bertin & Arnouts 1996) for the images stacked with SWarp, using the following parameters for the detection: DETECT_MINAREA=5., DETECT_THRESH=1.5, BACKSIZE=16, BACK_FILTERSIZE=3. These parameters correspond roughly to the S/N cut of 3.4. From the background noise, we estimate that the $5\text{-}\sigma$ detection limit of sources over $7''.0$ diameter aperture to be $60 \mu\text{Jy}$ or 19.5 AB magnitude.

The conversion to Jy unit and AB magnitude from the measured DN was done by applying the flux conversion factor provided in the IRC manual version 1.1, released on 2007 March 22. When converting DN to flux, we also applied the color correction factor provide in the IRC manual since the color correction can change the flux value by as much as 30% in some cases. The application of the color correction is not straightforward because of the complex shape of the spectral energy distribution of $11 \mu\text{m}$ sources. The IRC manual provide the color correction for black body with various temperatures. As a first-order approximation, we adopted the color correction factor of a black body with the temperature which matches the observed color of the object at the wavelengths of the passband in question and the passband closest to it. For example, the color correction factor of S7-band is derived by matching the observed S7-S9W color with the same color of a black body. For N3 and S7, we adopted the mean of the color correction factors derived from N2-N3/N3-N4 and S7-S9W/S9W-S11 respectively. With the color correction factor, we estimate the accuracy of the flux calibration to be roughly 15 % from stellar spectra (see Section 4.4).

Not all of the detected sources are real objects, and our test of the reliability of source detection on the negative image – the S11 image that has been multiplied by -1 – shows that there are spurious sources even at a very bright magnitude due to several instrumental effects such as imperfect flat image. Therefore, we excluded spurious sources manually by checking the S11 detection against the AKARI NIR images and CFHT optical images for objects brighter

¹ http://terapix.iap.fr/rubrique.php?id_rubrique=49

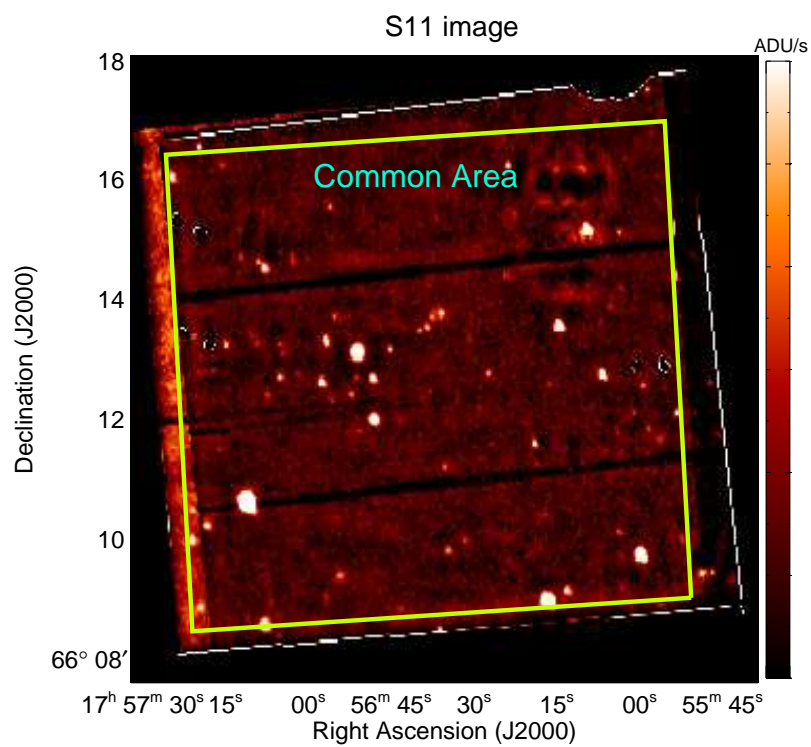
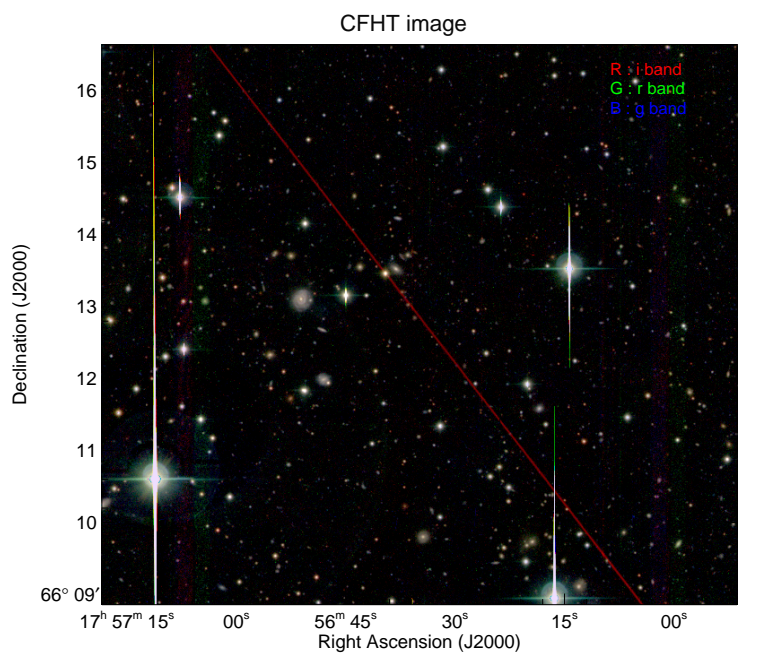


Fig. 2. The RGB representation of CFHT image (upper panel) and the master image which was produced by combining all exposures with S11 filter. The total exposure time for S11 image image is about 10 minutes.

than 19 AB mag objects. If an S11 detection accompanies detection in none of the AKARI NIR and the CFHT bands, we considered the source detection to be spurious. Detection in the shorter MIR-S bands alone is not considered to be true, since they can be ghost images from the shared MIR-S optics. After the manual inspection, the final list of S11 sources includes 176, among which 113 are brighter than 19.0 mag.

We use the AUTO-magnitude from the SExtractor for the S11 flux. We have compared the auto-magnitude against aperture magnitude with ~ 7.2 arcsec diameter and an aperture correction derived from the growth curve, and found a reasonable agreement between the two. When there are close neighbors that could affect the AUTO-magnitude (i.e., the source being likely to be blended one), we used the aperture magnitude with the aperture diameter of $7''.2$. Based on the $11\ \mu\text{m}$ -selected sample, we have produced a band-merged catalogue as follows. In order to measure fluxes in the other IRC bands, we used ASSOC_parameters in SExtractor. Fluxes were measured at the position of each object over the same area used for the S11 flux measurement, after finding the nearest counterpart within $4''.0$ radius. In case of the CFHT optical bands, $11\ \mu\text{m}$ source catalog was matched with the CFHT catalog with a matching radius of $3''.0$. The matching shows that almost all of the matched CFHT sources lie within $2''.0$ from the S11 position. When multiple objects are matched for a single S11 source, images were examined by eyes to find the most probable object that is responsible for the $11\ \mu\text{m}$ detection. Since the PSF shape varies among different AKARI passbands, our procedure may introduce additional error in the flux measurement at passbands below $11\ \mu\text{m}$. We have checked whether such an error is significant by performing the SExtractor detection and flux estimate on NIR images, and comparing the resultant AUTO-flux with the flux measured through the above procedure. We find that the additional uncertainty introduced by the above flux estimate to be less than 10%.

We have divided the detected sources at $11\ \mu\text{m}$ into stellar and non-stellar sources, based on the cross identification with the CFHT data. Through visual inspection, we classified an object as a star when the object has a clear trace of point sources such as diffraction spikes and has the minimal FWHM width. The stellarity values are checked for the sources that appear to be a point source.

Table 2. List of Sources brighter than $S_{11} = 18.5^m$

Id	RA	Dec	N2	N3	N4	S7	S9W	S11	Type
(1)	(2)	(3)	(4)	(5)	(6)	(7)	(8)	(9)	(10)
J175545.68+661144.7	268.94034	66.1958	19.93	19.89	19.94	20.5	19.8	18.1	SF Galaxy
J175546.49+660926.2	268.94373	66.1573	18.38	18.47	18.90	17.9	18.0	17.3	SF Galaxy
J175546.64+661236.8	268.94434	66.2102	18.90	19.11	20.10	19.4	19.1	17.9	SF Galaxy
J175548.42+660925.6	268.95175	66.1571	18.78	18.86	19.06	19.0	*	18.0	SF Galaxy
J175552.03+661000.7	268.96680	66.1669	19.56	19.82	20.11	18.1	17.0	16.5	SF Galaxy
J175552.67+661421.6	268.96948	66.2393	17.55	17.80	18.23	18.3	17.6	17.0	SF Galaxy
J175552.76+661205.8	268.96985	66.2016	18.53	18.86	19.17	18.7	17.6	17.2	SF Galaxy
J175556.06+661139.1	268.98361	66.1942	19.83	19.78	20.11	*	19.0	17.8	SF Galaxy
J175556.11+661343.1	268.98380	66.2286	19.42	19.60	19.76	19.4	18.1	18.1	SF Galaxy
J175556.59+661539.9	268.98581	66.2611	20.92	21.16	20.99	*	19.7	18.4	SF Galaxy
J175558.04+661150.8	268.99185	66.1975	17.58	17.81	18.46	19.5	18.8	18.0	SF Galaxy
J175559.06+661235.0	268.99612	66.2097	18.77	18.89	19.17	20.1	19.2	17.8	SF Galaxy
J175559.52+660944.2	268.99802	66.1623	17.02	17.25	17.45	*	16.1	14.8	SF Galaxy
J175602.13+661620.2	269.00888	66.2723	19.78	19.84	20.59	*	19.8	18.3	SF Galaxy
J175603.06+660912.4	269.01279	66.1534	19.45	19.70	20.15	20.4	18.4	18.4	SF Galaxy
J175603.45+661506.5	269.01440	66.2518	19.16	18.77	19.03	18.9	18.7	18.2	SF Galaxy
J175603.58+661007.7	269.01492	66.1688	19.01	19.15	19.47	18.2	17.6	18.5	SF Galaxy
J175606.54+661129.6	269.02728	66.1916	17.14	17.48	18.43	18.7	19.3	18.3	Star
J175606.58+661244.6	269.02744	66.2124	18.66	17.85	17.54	16.6	16.5	16.2	AGN
J175609.47+661508.9	269.03949	66.2525	17.38	16.69	16.58	15.9	15.6	15.4	AGN
J175613.04+660907.8	269.05438	66.1522	16.34	16.48	17.19	17.6	17.4	16.7	SF Galaxy
J175614.60+661332.0	269.06085	66.2256	12.79	13.18	13.83	14.7	15.2	15.6	Star
J175616.01+661235.3	269.06674	66.2098	20.20	19.68	19.60	19.5	19.7	18.2	SF Galaxy
J175617.63+660951.6	269.07349	66.1643	18.77	18.11	19.82	18.6	*	18.2	Early-type
J175618.63+661136.6	269.07764	66.1935	18.31	18.61	19.00	18.2	17.4	17.4	SF Galaxy
J175622.40+661525.4	269.09338	66.2570	19.10	19.19	19.46	19.0	17.8	17.6	SF Galaxy
J175623.97+661423.9	269.09988	66.2400	15.38	15.87	16.57	17.7	18.7	18.3	Star
J175623.98+661613.6	269.09992	66.2705	18.07	18.34	18.78	19.6	17.5	17.8	SF Galaxy
J175624.41+661641.5	269.10172	66.2782	19.73	19.40	19.49	19.7	19.5	18.3	SF Galaxy
J175627.10+661245.3	269.11295	66.2126	21.89	21.75	20.22	18.6	18.4	17.8	Early-type
J175631.06+661653.8	269.12946	66.2816	16.57	17.00	17.54	18.6	19.0	18.4	Early-type
J175631.47+660958.9	269.13117	66.1664	19.78	19.75	20.01	20.4	*	18.4	SF Galaxy
J175634.29+660846.9	269.14288	66.1464	15.69	16.26	16.95	*	16.9	17.7	Star
J175634.44+660949.3	269.14352	66.1637	16.84	17.11	17.81	18.8	17.6	16.5	SF Galaxy
J175635.13+661112.9	269.14639	66.1869	20.02	19.90	20.50	20.8	19.7	18.0	SF Galaxy
J175635.94+660824.2	269.14975	66.1401	13.58	13.36	13.77	14.4	15.7	16.3	Star
J175637.53+661342.9	269.15640	66.2286	17.01	16.98	17.44	17.2	17.6	18.1	early-type
J175639.09+661547.2	269.16290	66.2631	17.86	18.40	18.83	19.6	*	17.7	SF Galaxy
J175639.80+661328.8	269.16583	66.2247	15.31	15.73	16.40	17.4	17.9	18.5	Star
J175643.10+660850.4	269.17960	66.1473	19.46	19.83	19.90	*	18.2	17.5	SF Galaxy
J175645.21+661310.5	269.18839	66.2196	14.70	15.16	15.85	16.9	17.2	18.0	Star
J175648.21+661200.1	269.20090	66.2000	16.61	17.04	17.55	17.1	16.4	16.2	SF Galaxy

Table 2 – continued

Id	RA	Dec	N2	N3	N4	S7	S9W	S11	Type
(1)	(2)	(3)	(4)	(5)	(6)	(7)	(8)	(9)	(10)
J175648.43+661241.7	269.201843	66.2116	18.12	18.48	18.54	18.0	17.1	16.8	SF Galaxy
J175651.33+661307.2	269.213898	66.2187	15.43	15.83	16.24	16.2	15.3	15.1	SF Galaxy
J175651.45+661242.5	269.214386	66.2118	20.06	20.26	19.58	19.2	19.4	18.4	AGN
J175652.34+661225.3	269.218109	66.2070	20.38	19.96	20.31	19.5	18.6	17.9	SF Galaxy
J175654.21+660924.1	269.225891	66.1567	18.92	18.89	19.48	18.2	17.6	17.2	SF Galaxy
J175655.07+661343.7	269.229462	66.2288	18.09	18.27	18.90	19.0	18.6	18.0	SF Galaxy
J175655.97+661534.1	269.233246	66.2595	20.39	19.71	19.29	18.7	17.9	17.9	AGN
J175656.50+661316.0	269.235413	66.2211	19.06	18.95	19.11	17.5	17.3	16.6	SF Galaxy
J175657.46+661237.6	269.239441	66.2105	18.08	18.37	18.73	18.6	17.0	16.6	SF Galaxy
J175658.82+660834.6	269.245117	66.1429	18.31	18.45	18.88	18.5	18.2	17.9	SF Galaxy
J175702.81+661439.5	269.261749	66.2443	19.36	19.22	19.43	19.7	18.7	18.0	SF Galaxy
J175704.53+661304.9	269.268890	66.2180	18.13	18.36	18.95	19.7	18.9	18.4	SF Galaxy
J175705.12+661242.2	269.271362	66.2117	18.72	18.44	18.64	18.4	18.3	17.6	SF Galaxy
J175705.16+661316.2	269.271515	66.2212	18.37	18.60	19.20	20.0	*	18.1	SF Galaxy
J175707.37+661224.7	269.280731	66.2069	15.51	15.96	16.65	17.8	18.0	17.6	Star
J175707.81+660833.9	269.282562	66.1427	16.08	16.60	17.13	*	*	16.1	SF Galaxy
J175708.01+660928.6	269.283386	66.1579	19.72	19.20	19.40	18.4	17.5	18.2	SF Galaxy
J175708.04+661431.5	269.283508	66.2421	13.96	14.45	15.08	15.8	16.5	17.0	Star
J175709.08+661439.2	269.287872	66.2442	15.21	15.73	16.46	*	*	17.8	Star
J175710.35+661324.3	269.293152	66.2234	16.34	16.61	16.83	18.0	18.0	17.5	SF Galaxy
J175712.35+661442.9	269.301483	66.2453	18.74	19.04	19.44	19.5	18.6	18.4	SF Galaxy
J175715.07+661315.0	269.312805	66.2208	18.41	19.07	19.24	18.4	18.8	17.4	SF Galaxy
J175715.88+661614.8	269.316193	66.2708	19.58	19.29	19.68	20.9	18.8	17.4	SF Galaxy
J175716.24+661131.3	269.317688	66.1920	15.58	15.97	16.65	17.8	17.7	18.2	Star
J175718.52+661014.4	269.327210	66.1707	16.13	*	17.14	17.3	17.5	16.9	SF Galaxy
J175719.70+660852.0	269.332092	66.1478	18.16	*	18.27	18.7	*	17.4	SF Galaxy
J175720.25+661630.9	269.334412	66.2753	14.45	14.97	15.65	16.7	17.5	17.9	Star
J175721.28+660959.0	269.338684	66.1664	14.42	*	15.90	16.4	17.2	17.4	Star
J175725.25+661602.0	269.355225	66.2672	16.88	*	17.85	18.6	17.7	16.9	SF Galaxy
J175728.03+661530.0	269.366791	66.2583	20.47	*	*	*	*	18.1	SF Galaxy

(1) ID of the object; (2) RA and DEC in J2000; (3)-(9): AB magnitudes at these bands; (10) Object type: SF Galaxy for star forming galaxy (Section 4.3.1), Early-type for a galaxy with E/S0-like spectra (Section 5), Star for point source with stellar spectra (Section 4.3.3), and AGN for power-law sources which are likely to be AGNs (Section 4.3.2).

4. RESULTS

4.1. S11 Number Count and the Magnitude Limited Sample

The number count of S11 sources as a function of AB magnitude is shown in Fig. 3. The total count (black histogram) as well as the count for non-stellar objects only (red histogram) are shown together. The expected distribution of sources uniformly distributed over the sky in a non-expanding, Euclidean universe is indicated as a straight line with slope of 0.6. The observed

source count peaks at around 19-th magnitude and declines afterward. Clearly, we encounter the incompleteness effect beyond 19-th magnitude. In order to investigate the incompleteness in our sample, we created artificial objects that have a Gaussian PSF shape with the FWHM value of the point sources in the S11 image. We distributed them in less crowded parts of the S11 image and performed the source detection. From this exercise, we find that our source counts is nearly complete down to $S11 \sim 18.5$ mag ($> 90\%$), while it drops to 50% level at 19.2 mag.

Our visual inspection of S11 image also confirms that the number of spurious sources increases as we go to $S11 > 18.5$ mag. Therefore, we consider a sample with $S11 < 18.5$ mag to be highly complete and reliable, and use this sample of 72 objects to characterize the property of S11 sources. The AB magnitudes of our sample are listed in Table 2, together with our identifications regarding the type of the objects from the SED shape as well as the appearance of the object. We have classified our sources into 4 categories: stars, star forming galaxies, early type galaxies, and AGNs. We also add a supplemental sample made of sources fainter than $S11 = 18.5$ mag, but have spectral energy distributions worth of special note. These sources are treated separately in §5. We concentrate on the flux limited sample at $11 \mu\text{m}$ in this section.

4.2. Colors

The S7-S11 versus N2-N4 color-color diagram of the $11 \mu\text{m}$ flux limited sample is shown in Fig. 4. The sources identified as stars are indicated as asterisks while non-stellar sources are shown as filled dots with different sizes depending on the brightness. Also shown in this diagram is the same color-color sequences of three typical nearby star forming galaxies M51, M82 and Arp 220 located at redshifts in the range between $z = 0$ and 2.2. It is clear from this figure that most of the S11 flux limited sources found in a shallow NEP survey are likely to be star forming galaxies at low to medium redshifts. However, there are also redder sources in N2-N4 color index than star forming spiral galaxies. As we shall see, most of them are AGN.

The N4 versus N4-N2 and N4 versus N4-N3 color-magnitude diagrams are shown in Fig. 5. In near infrared, the stellar SEDs are nearly that of Rayleigh Jeans tail of black body, and therefore stars lie in rather narrow range in this diagram. Also shown as solid and dashed lines are locations of an L^* galaxy having the SED shape of M51 and M82, respectively, at different redshifts as marked on the lines. Actual data points are consistent with the star forming disk galaxies lying within the redshift $\lesssim 1$. Again, the objects with very red color in N2-N4 are likely to be AGNs. Such red objects are more easily distinguished in N2-N4 than N4-N3.

4.3. Characteristics of the Magnitude-limited Sample

So far we have been investigating the general properties of the $11 \mu\text{m}$ selected sources. We now take a closer look at individual sources. Based on the SEDs, we divide our sources into three categories: stars, galaxies, and AGNs.

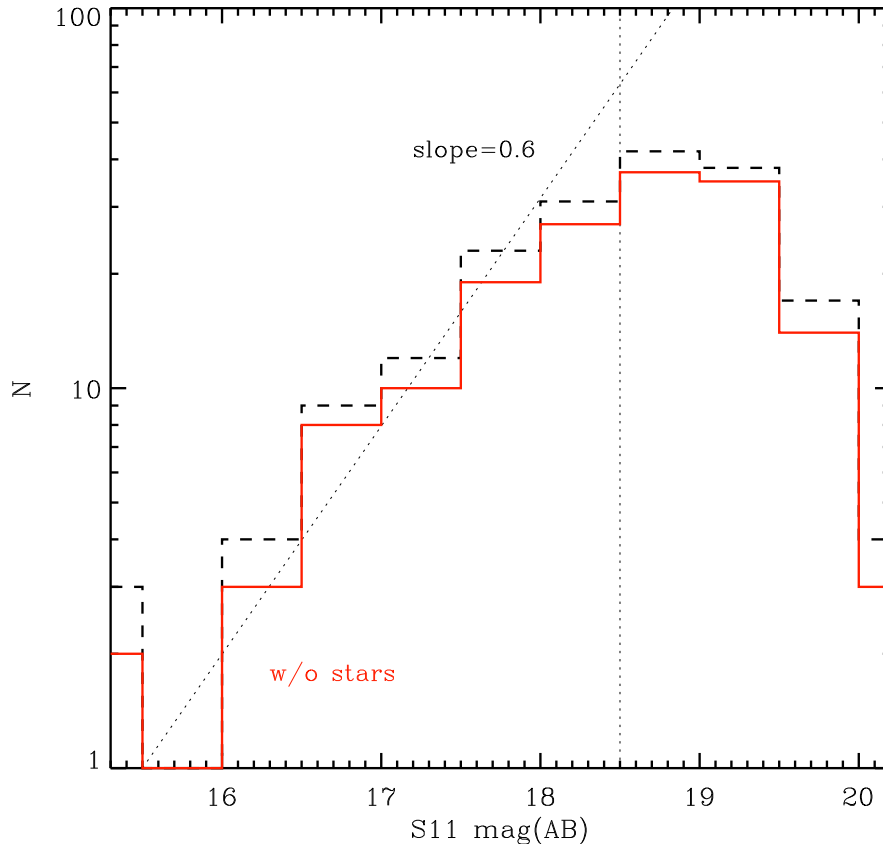


Fig. 3. The number distribution of S11 sources as a function of magnitude. Both total sources as well as non-stellar sources are plotted. At bright end, the number count approximately follows the $N \propto m^{0.6}$ power-law, but begins to deviate as the incompleteness becomes important at around 19-th magnitude. The stellar sources comprise only small fraction of the entire sample.

4.3.1. Galaxies

We identified galaxies from their spectral shapes, and their morphological appearances in the CFHT image. The galaxies are further divided into star-forming galaxies and early type galaxies based on their SED shapes. The total number of objects identified as star forming galaxies is 50, corresponding to about 70% of the total S11 selected sample, while only five objects are classified as early-types. Fig. 6 shows SEDs of a representative set of star-forming galaxies at $S11 < 18.5$ mag, as well as postage stamp images of these galaxies. The SEDs are matched with 100 SED templates IR luminous galaxies in Chary & Elbaz (2001), using the Bayesian photometric redshift code of Benitez (2000). By doing so, we obtain an estimate of photometric redshift as well as the best-fit SED template. Infrared luminosity is then calculated by integrating the fluxes beyond the rest-frame $5 \mu\text{m}$ of the best-fit SED template, and rescaling the value according to the luminosity distance. The best-fit SED template is plotted over the observed points in Fig. 6, and we also indicate the photometric redshift in each panel. The

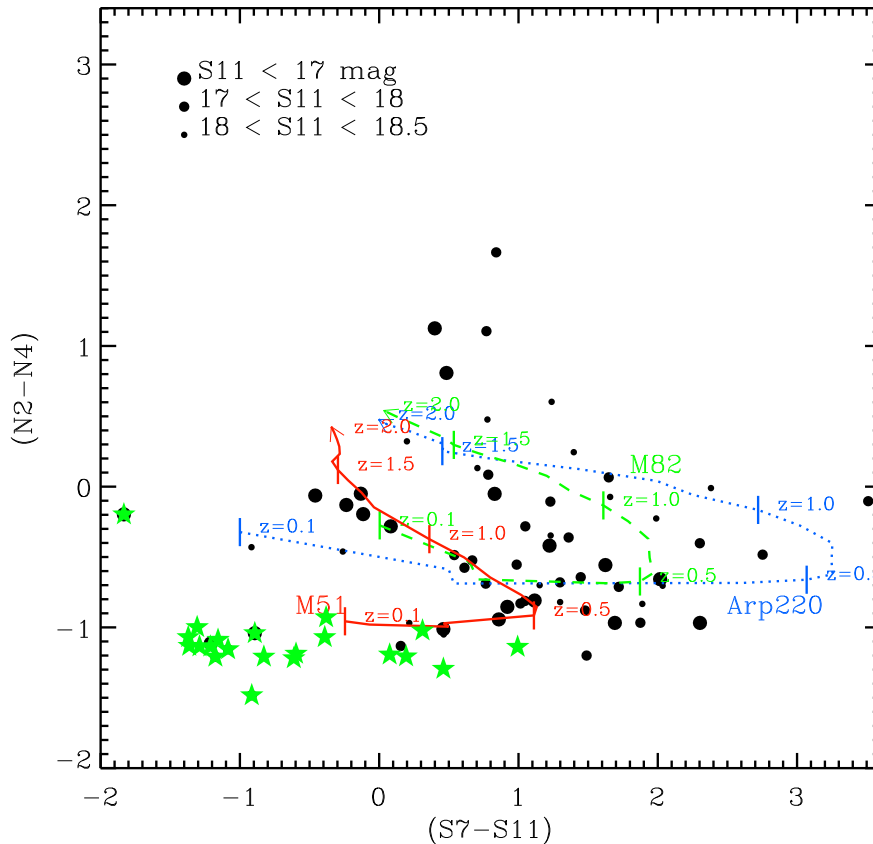


Fig. 4. The S7-S11 versus N2-N4 color-color plots of the S11 flux limited sample. The stars are located in the lower-left corner (green star symbols). Also shown in this diagram are the sequence of three star forming galaxies M51, M82 and Arp 220 at redshifts from $z=0$ to 2.2. Majority of the non-stellar sources are likely to be galaxies at low to moderate redshifts. AGNs occupy the upper right part of the color-color diagram because of their power-law SEDs.

probability distribution of photometric redshift is also given in the panel next to the SED plot. When performing the SED-fit, note that we have added photometric uncertainties of 10% for NIR, 15% for S7 bands, and 20% for S9W and S11 bands in order to account for the uncertainties in different bands that we have found when fitting stellar spectra (see Section 4.3.3). The star forming galaxies in general have SEDs that hump at the rest-frame $1.6 \mu\text{m}$, and also have strong MIR emission in excess of the stellar light expected from the Rayleigh-Jeans tail of the black body radiation. Fig. 6 demonstrates that the S9W and S11 data points are crucial for sampling the redshifted excess MIR emission and the rest-frame $7.7 \mu\text{m}$ and $6.2 \mu\text{m}$ PAH features for those located at $z \gtrsim 0.2$. We expect that the majority of S11 or S9W selected sources in shallow surveys of AKARI would be star forming galaxies of this kind. Fig. 7 shows the SEDs of all of the objects classified as star-forming galaxies which are brighter than 17.5 magnitude at S11, except for the cases where AKARI fluxes are confused with their neighbors

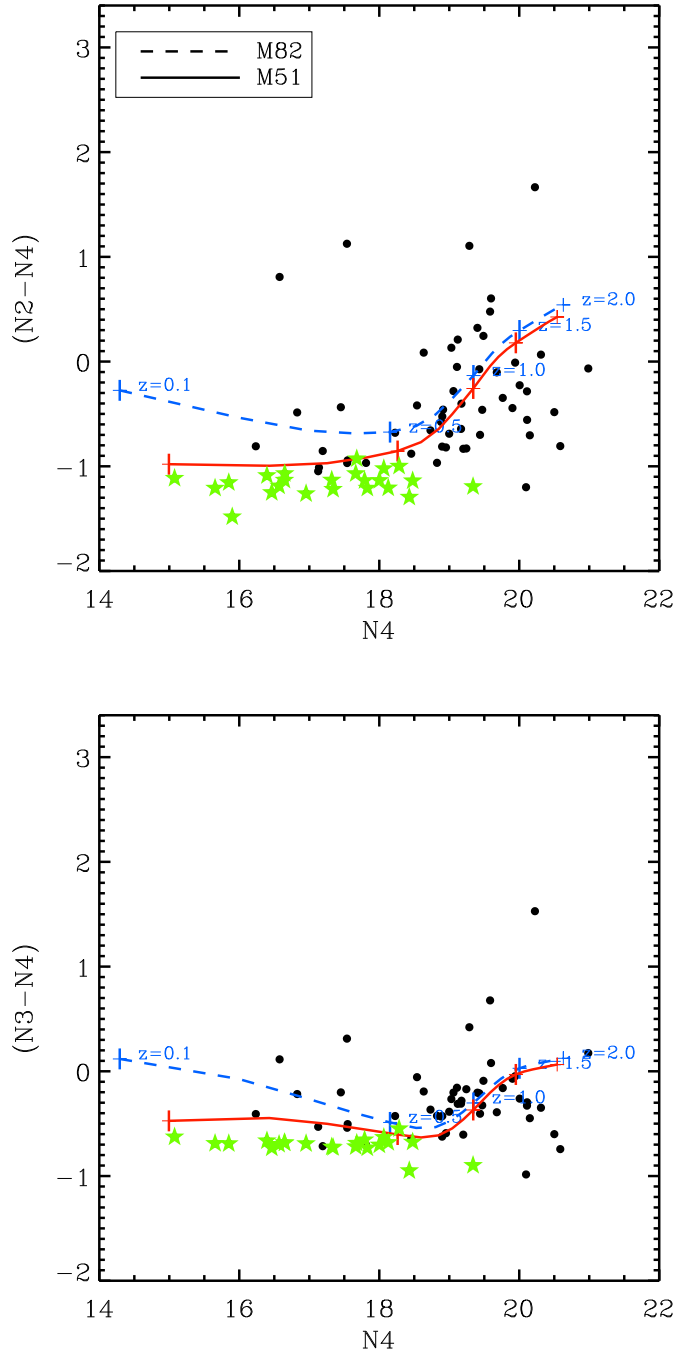


Fig. 5. The N2-N4 versus N4 and N3-N4 versus N4 color-magnitude diagrams. The sources identified as stars are marked as green stars. The stars lie very narrow ranges in N2-N4 and N3-N4 colors while extragalactic objects show much broader distribution. Very red objects in N2-N4 color are likely to be AGNs. The locations of star forming disk galaxies at different redshifts are also shown as solid and dashed lines. We may conclude that the majority of the sources shown in these diagrams are star forming disk galaxies at low to medium redshifts.

(multiple sources). Like the example SEDs given in Fig. 6, the SEDs of 11 μm selected galaxies can be characterized by a broad peak in near infrared and brightening at mid infrared. The mid infrared flux can be attributed mostly to the warm dust with PAH emission features. The SED fitting to these objects shows that they have IR luminosity of order of $L_{IR} \sim 10^{10} - 10^{12} L_{\odot}$, in the regime of the LIRGs. We also find that the majority of the objects have photometric redshifts of $0.2 \lesssim z \lesssim 0.7$.

4.3.2. AGNs

Among the S11 selected sample, we identify 4 objects ($\sim 6\%$) with power-law SEDs which are commonly found for AGNs (e.g., Alonso-Herrero et al. 2006). We classify these objects to be AGNs. In particular, two of these objects have been detected in X-ray, and classified as AGNs from their X-ray flux as well as their optical spectra (J175609.47+661508.87 at $z = 0.6357$ and J175651.45+661242.47 at $z = 1.425$; Gioia et al. 2003; Henry et al. 2006). The SEDs of all four ($\sim 6\%$) sources as identified as AGN are shown in Fig. 8. Their IR SEDs are fitted with a power-law function ($f_{\nu} \sim \nu^{\alpha}$), and we find that the power-law index of these AGNs to be in the range of $-1.5 < \alpha < -0.9$, similar to that of QSOs and AGNs such as Mrk231 (Elvis et al. 1994; Ivezić et al. 2002; Alonso-Herrero et al. 2006).

4.3.3. Stars

Among 72 sources with S11 magnitude brighter than 18.5 magnitude, 14 ($\sim 19\%$) are found to be stars. The selection of the stellar sources are done by inspecting the cross identified CFHT images. These are further confirmed by plotting the SEDs. The typical stellar SEDs are shown in Fig. 9. The optical images are often saturated, at their center, therefore, we did not include optical fluxes in Fig. 9. All the objects classified as stars have a steeply declining SED shape toward the longer wavelengths, which are consistent with the Rayleigh-Jeans tail of the black body radiation. Also plotted in Fig. 9 is a black-body fit of the IR spectra. The figure demonstrates that the blackbody fit is reasonable. The figure also demonstrates the effect of the application of color-correction factor on photometric data points. The X-marks in Fig. 9 indicate the data point before the color correction. Without the color correction, the N4 flux is underestimated by 30%, but the color correction reduces the systematic error to 10-15% level (see also Takagi et al. 2007). From these fits to the stellar spectra, we estimate the systematic uncertainty in NIR-bands and S7-band fluxes and to be $\sim 10\%$. For S9W and S11-bands, the uncertainty seems to be larger ($\sim 15\text{-}20\%$).

5. Additional 11 μm Sources

We found several interesting sources that are beyond our magnitude cut of 18.5 mag. Here, we discuss these objects. SEDs and multi-band postage stamp images of these objects are given in Fig. 10, respectively.

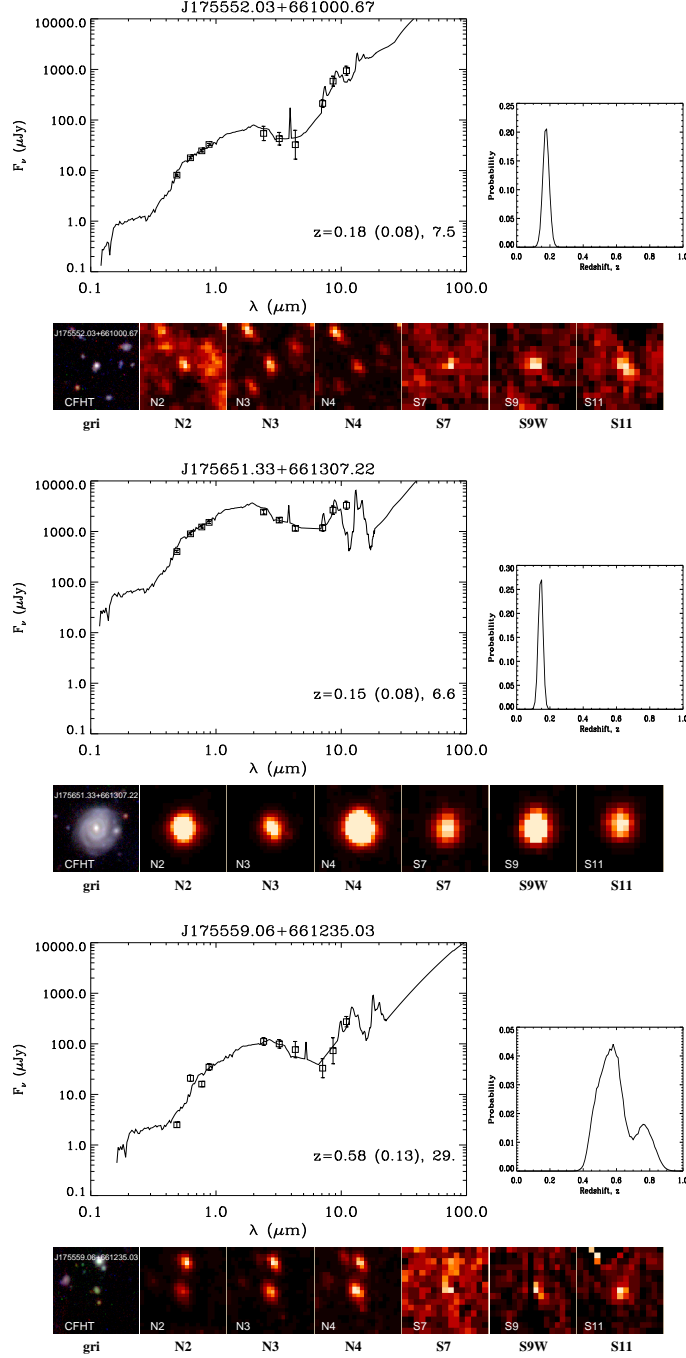


Fig. 6. The SED fitting of three star-forming galaxies: Redshifts are indicated in each picture, with their $1\text{-}\sigma$ uncertainty shown in the parenthesis. The number next to the redshift is the luminosity in units of $10^{10} L_\odot$. For the IR luminosity, we estimate the uncertainty to be at least a factor of a few. Majority of the sources classified as star-forming galaxies lie in $0.2 \lesssim z \lesssim 0.7$ with luminosity ranging from 10^{10} to $10^{11} L_\odot$.

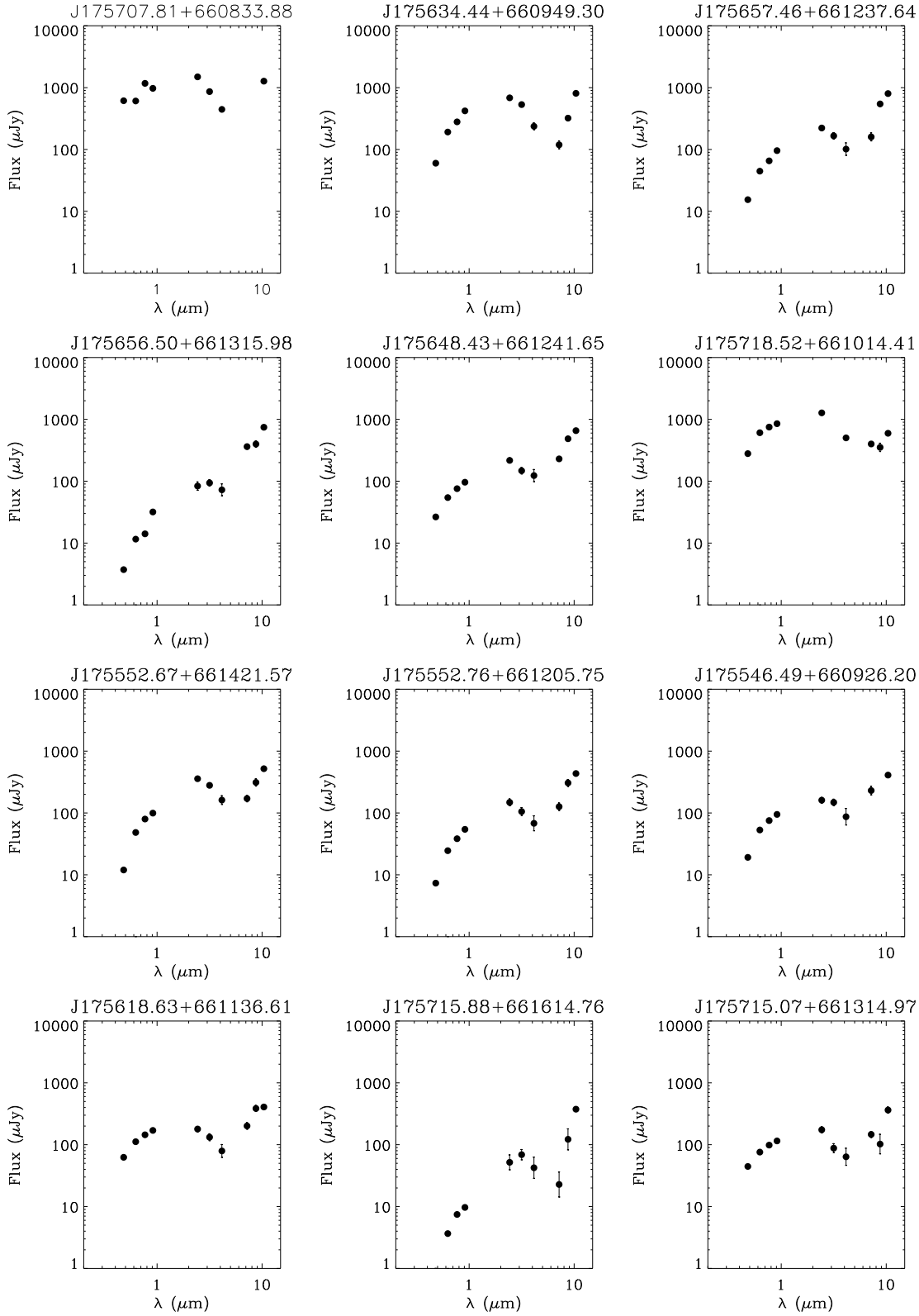


Fig. 7. Optical to mid infrared SEDs of 12 brightest sources that are classified as star forming galaxies based on the inspection of CFHT image. We have excluded the sources whose mid-infrared fluxes might have been contaminated by the nearby sources. Out of 72 sources, 50 fall in this category. The SEDs are characterized by broad peak at optical or near infrared followed by brightening of mid infrared fluxes.

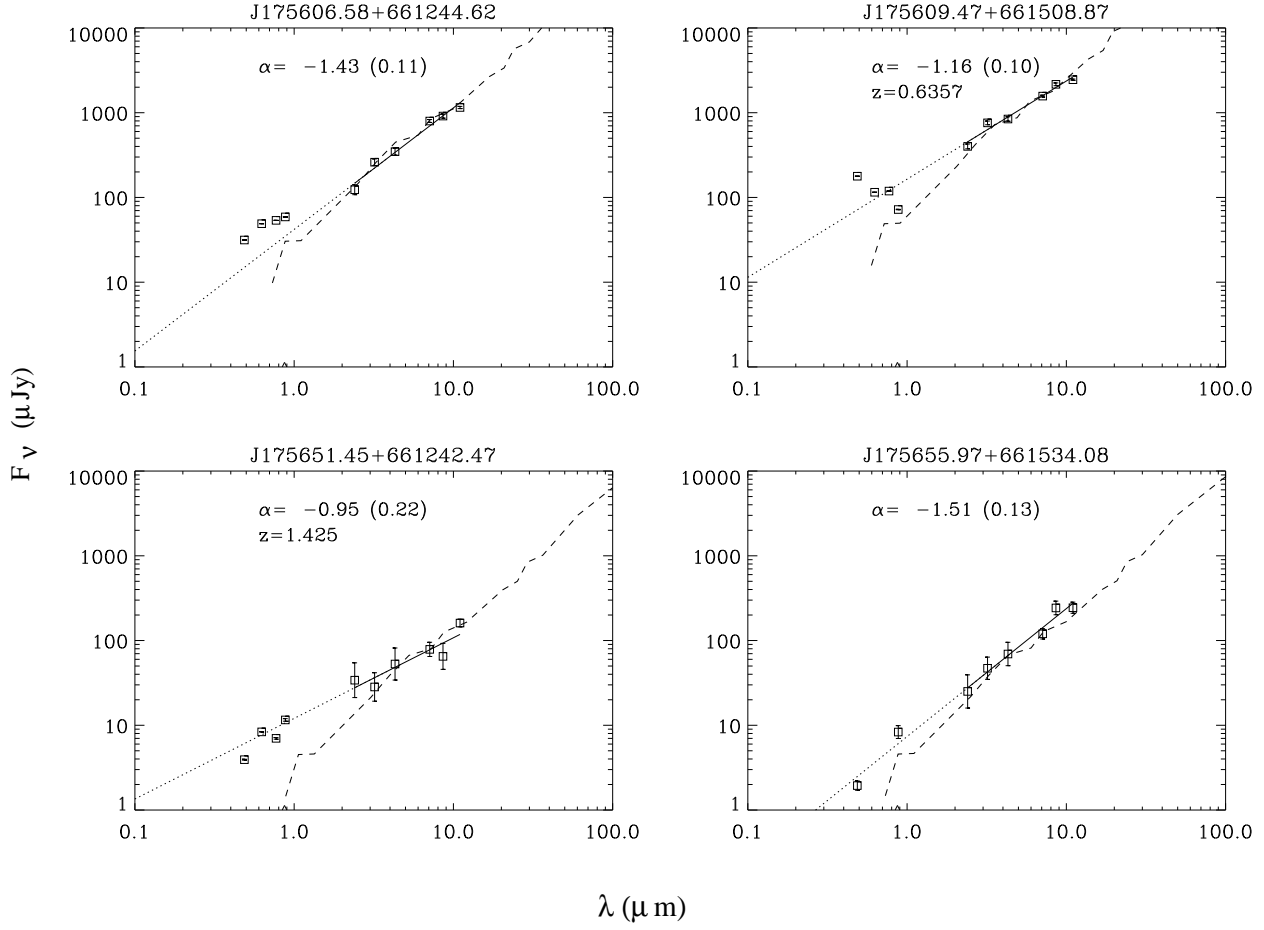


Fig. 8. The SEDs of four sources which are classified as ‘AGNs’. One of them is an X-ray source located at $z = 0.6357$ (J175609+661509), and another one is J175651.45+661242.47 at $z = 1.425$. Also drawn in the figure are a redshifted SED of Mrk231 normalized at the observed $7 \mu\text{m}$ flux as the dashed line (to the corresponding spectroscopic redshift, or $z = 1$ if there is no z_{spec}), and the power-law fit to the observed NIR+MIR SED points (solid and dotted lines). The power-law index, α (see the text), is also indicated in each figure with its error shown in the parenthesis. The optical image around this source shows overdensity of faint galaxies which might be members of the cluster of galaxies at this redshift.

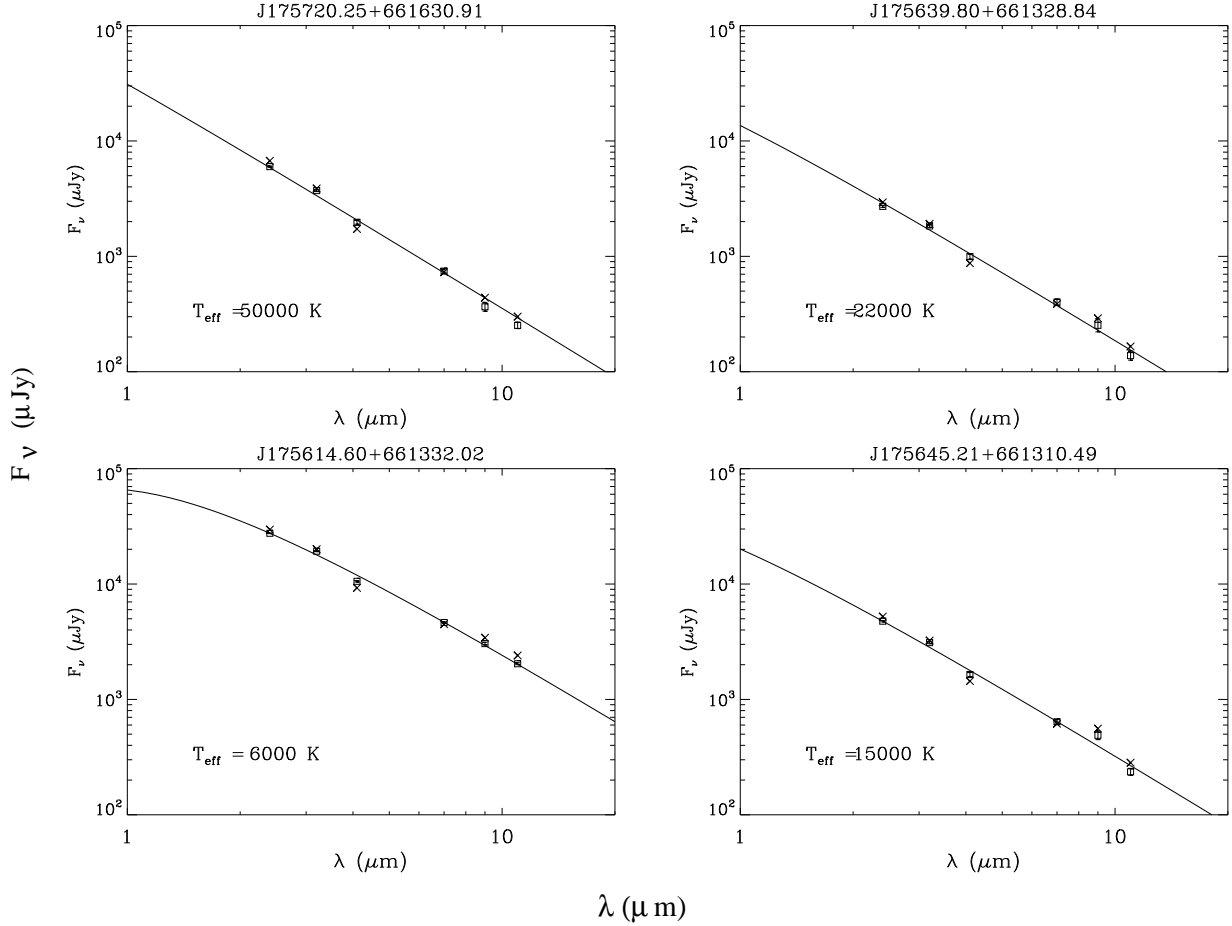


Fig. 9. The SEDs of four sources which are classified as ‘stars’ based on the close inspection of CFHT image (squares). Most of them are well fitted by the black body SED of temperatures ranging from 6000 K to 50000 K. The size of each square represents roughly 10% error. X-marks indicate the photometric data before color-correction. The color correction helps reduce the dip in N4-band.

5.1. Brown Dwarf Candidate

We find that an object J175620.85+661435.5 has a very red optical color, and a very compact appearance in the CFHT image. When combined with the AKARI N2, N3, N4, S7, and S9W data, its SED can be fitted well with that of a black body with the surface temperature of $T_{eff} \simeq 2500$ K (dashed line). The observed SED also resembles that of a L0V-type star, 2MASS J03454316+2540233 (solid line; Kirkpatrick et al. 1999; McLean, et al. 2003). The overall shape of the SED is very hard to fit with SEDs of extragalactic sources, thus, we consider J175620.85+661435.5 as a strong candidate to be a brown dwarf. Current limits on fluxes longward of $7 \mu\text{m}$ have large uncertainties. To be able to say if this object has a circumstellar disk like some brown dwarfs (Riaz et al. 2006; Luman et al. 2005), we require a deeper data which we expect to accumulate at the end of the NEP survey.

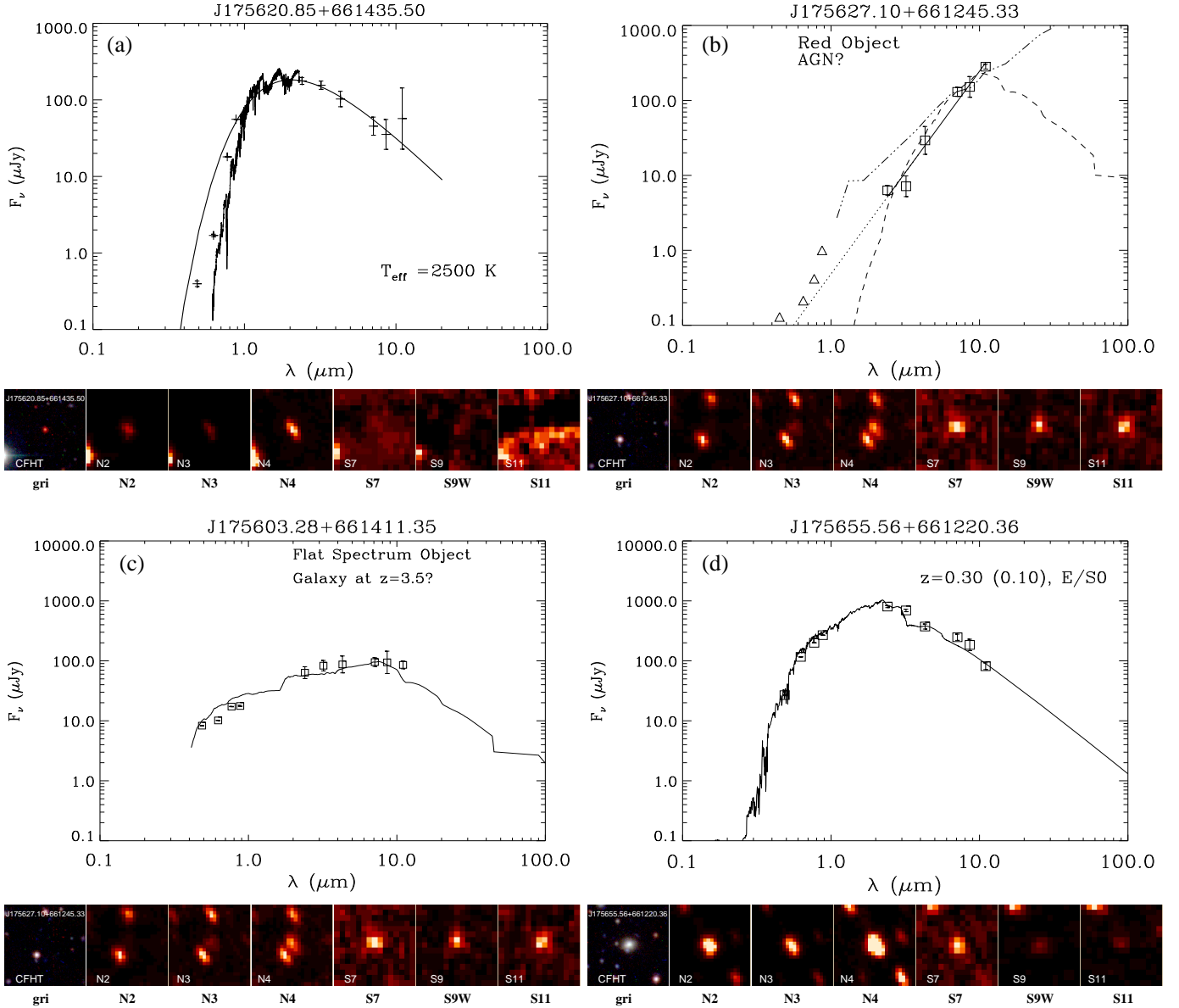


Fig. 10. The spectral energy distributions of interesting, faint $11\ \mu\text{m}$ sources. From the upper-left to the clockwise direction, a brown dwarf candidate (a), a dusty-AGN (b), a flat-spectrum object (c), and an E/S0 at $z = 0.3 \pm 0.1$. (d). The $4\text{-}\sigma$ detection limits of CFHT image are also plotted as triangles. Also plotted below each figure is the postage stamp image of the object (*gri*-color composite of CFHT image, N2, N3, N4, S7, S9W, and S11 from left). The size of each postage stamp image is $30''0 \times 30''$.

5.2. J175627.10+661245.33: Peculiarly red object

We find in this field, an extremely red object, J175627.10+661245.33, which is not detected in all of the optical bands but is visible in N2 through S11. Fig. 10b shows the postage stamp image of this galaxy as well as its SED. Since they are visible in all the AKARI bands, we believe that the detection of this object is secure. The optical-NIR color of J175627.10+661245.33 is $(i - N2)_{AB} \gtrsim 6$, and $(R - N2)_{AB} > 6.7$, placing it to be one of the reddest EROs and also possibly a Hyper-Extremely Red Object (HERO; e.g., Im et al. 2002). The most likely explanation for the nature of this source is that it is a dust-obscured AGN. The power-law slope of this object is $\alpha \sim -2.8$ where α is defined as $f_\nu \sim \nu^\alpha$. The power-law sources, which are dominated by AGNs, have the power-law slopes of $\alpha = -0.5 \sim -2.8$ (Alonso-Herrero et al. 2006). This object qualifies to be in such a category. The spectral energy distribution of J175627.10+661245.33 can be also fitted by that of (i) a heavily dust-extinct star forming galaxy at $z > 5$ (dashed-line); or (ii) a few hundred Myr object at $z \sim 9.5$. The case (ii) is unlikely, since the estimated stellar mass for such an object exceeds above $10^{13} M_\odot$.

5.3. Flat spectrum source

We find that J175603.28+661411.35 to be a source which has a nearly flat IR spectrum (Fig. 10c). The spectral slope of the IR points is $\alpha \sim 0.23$, which is too flat to be a typical AGN ($-2.8 < \alpha < -0.5$; Ivezić et al. 2002; Alonso-Herrero et al. 2006). The flat IR spectrum and the detection at g' -band suggests that this could be a several hundred Myr, star-forming galaxy at $z \sim 3.5$ with a moderate amount of dust extinction ($E(B - V) \sim 0.1$), although this object could also be an AGN. The nature of this object is currently uncertain.

5.4. Early type galaxies

SEDs of several objects, not in the S11 sample, are found to be consistent with those of early-type galaxies at moderate redshift. Fig. 10d shows one such example at the estimated distance of $z = 0.3 \pm 0.1$. Shown in the solid line is the spectrum of a 2.5 Gyr-old passively evolving galaxy with the metallicity 2.5 times the solar value. No obvious excess in MIR beyond $7\mu\text{m}$ has been found for this object. The implication is that the dust emission from circumstellar material around AGB stars is minimal and that this early-type galaxy is at least a few Gyrs old from such a point of view (Piovan et al. 2003).

6. Summary

Using the AKARI IRC data near NEP that are obtained for the performance evaluation purpose, we have studied the nature of 11 μm selected sources. The field covers roughly $10' \times 10'$, and has a multi-wavelength imaging data in the CFHT g^* , r' , i' , and z' , and the AKARI N2, N3, N4, S7, S9W, and S11. The S11 source count from the stacked images of 2-3 pointing data shows that there are 72 objects at $S11 < 18.5$ mag, and that the source counts become

highly incomplete beyond $S11 > 19$ mag. We examine the nature of sources in the magnitude-limited sample of $S11 < 18.5$ mag, which we consider to be highly reliable and complete. We find that $\sim 68\%$ of the S11 sources are star-forming galaxies at $0.2 \lesssim z \lesssim 0.7$, whose PAH emissions redshifted into the S11 band. The early type galaxies comprise much smaller fraction ($\sim 6\%$) of the sample. We also classify $\sim 6\%$ of the S11 selected sources to be AGNs. The rest are found to be stars. We have also examined the nature of several interesting sources that are fainter than $S11 > 18.5$ mag. A brown dwarf candidate has been identified, as well as an Extremely Red Objects with no optical counterpart. We conclude that the AKARI S11 band is efficient for sampling and studying star-formation activity at moderate redshift, and other interesting sources such as AGNs and brown dwarfs.

AKARI is a JAXA project with the participation with ESA. The CFHT data used in this work are based on observations obtained with MegaPrime/MegaCam, a joint project of CFHT and CEA/DAPNIA, at the Canada-France-Hawaii Telescope (CFHT) which is operated by the National Research Council (NRC) of Canada, the Institut National des Sciences de l'Univers of the Centre National de la Recherche Scientifique of France, and the University of Hawaii. This work was supported in part by the KRF grant No. R14-2002-01000-0. MI and HS were supported by KOSEF grant No. R01-2005-000-10610-0. We thank the anonymous referee for useful suggestions.

References

- Alonso-Herrero, A., et al. 2006, ApJ, 640, 167
Benitez, N. ApJ, 536, 571
Bertin E., Arnouts S. 1996, A&AS, 117, 393
Chary, R.& Elbaz, D. ApJ, 556, 562
Elvis, M., et al. 1994, ApJS, 95, 1
Gioia, I. M., et al. 2003, ApJS, 149, 29
Hwang, N., et al. 2007, ApJS, in press
Henry, J. P., et al. 2006, ApJS, 162, 304
Im, M., et al. 2002, ApJ, 578, L19
Ita, et al. 2007, IRC Data User's Manual
Ivezic, Z., et al. 2002, AJ, 124, 2364
Kirkpatrick, D. J., et al. ApJ, 519, 802
Luhman, K. L., et al. 2005, ApJ, 620, L51
Matsuhara, H., et al. 2006, PASJ, 58, 673
Matsuhara, H., et al. 2007, PASJ, submitted
McLean, I. S., et al. 2003, ApJ, 596
Murakami H. 1998, Proc. SPIE, 3356, 471

- Nakagawa, T. 2001, in Pilbratt, G. L., Cernicharo, J., Heras, A. M., Prusti, T., Harris, R. eds. ESA SP-460, The Promise of the Herschel Space Observatory, ESA Publications Division, p. 67
- Onaka, T., et al. 2007, PASJ, submitted
- Oyabu, S., et al. 2007, PASJ, submitted
- Pearson C.P. 2001, MNRAS, 325, 1511
- Piovan, L., Tantalò, R., Chiosi, C. 2003, A&A, 408, 559
- Puget J.J., Lagache G., Clements D.L., et al. 1999, A&A, 345, 29
- Riaz, B., Gizis, J. E., & Hmiel, A. 2006, ApJ, 639, L79
- Rieke G. H. 1994, Detection of Light: from the Ultraviolet to the Submillimeter (Cambridge: Cambridge University Press)
- Rowan-Robinson M. 2001, ApJ, 549, 745
- Shibai H. 2004, Adv. Spce Res. 345, 584
- Silva, L., Granato, G. L., Bressan, A., & Danese, L., 1998, ApJ, 509, 103
- Takagi, T. et al. 2007, PASJ, submitted.
- Wada, T. et al. 2007, PASJ, submitted.